

In-plane uniaxial pressure-induced out-of-plane antiferromagnetic moment and critical fluctuations in BaFe₂As₂

Panpan Liu,^{1,*} Mason L. Klemm,^{2,*} Long Tian,¹ Xingye Lu,^{1,†} Yu Song,³ David W. Tam,² Karin Schmalzl,⁴ J. T. Park,⁵ Yu Li,² Guotai Tan,¹ Yixi Su,⁶ Frédéric Bourdarot,⁷ Yang Zhao,⁸ Jeffery W. Lynn,⁸ Robert J. Birgeneau,^{3,9,10} and Pengcheng Dai^{2,‡}

¹*Center for Advanced Quantum Studies and Department of Physics, Beijing Normal University, Beijing 100875, China*

²*Department of Physics and Astronomy, Rice University, Houston, Texas 77005, USA*

³*Department of Physics, University of California, Berkeley, California 94720, USA*

⁴*Forschungszentrum Jülich GmbH, Jülich Centre for Neutron Science at ILL, 71 avenue des Martyrs, 38000 Grenoble, France*

⁵*Heinz Maier-Leibnitz Zentrum (MLZ), Technische Universität München, 85748 Garching, Germany*

⁶*Jülich Centre for Neutron Science, Forschungszentrum Jülich GmbH, Outstation at MLZ, D-85747 Garching, Germany*

⁷*University Grenoble Alpes, CEA, IRIG, MEM-MDN Grenoble, France*

⁸*NIST Center for Neutron Research, National Institute of Standards and Technology, Gaithersburg, Maryland 20899, USA*

⁹*Materials Sciences Division, Lawrence Berkeley National Laboratory, Berkeley, California 94720, USA*

¹⁰*Department of Materials Science and Engineering, University of California, Berkeley, California 94720, USA*

(Dated: November 25, 2021)

A small in-plane external uniaxial pressure has been widely used as an effective method to acquire single domain iron pnictide BaFe₂As₂, which exhibits twin-domains without uniaxial strain below the tetragonal-to-orthorhombic structural (nematic) transition temperature T_s . Although it is generally assumed that such a pressure will not affect the intrinsic electronic/magnetic properties of the system, it is known to enhance the antiferromagnetic (AF) ordering temperature T_N ($< T_s$) and create in-plane resistivity anisotropy above T_s . Here we use neutron polarization analysis to show that such a strain on BaFe₂As₂ also induces a static or quasi-static out-of-plane (c -axis) AF order and its associated critical spin fluctuations near T_N/T_s . Therefore, uniaxial pressure necessary to detwin single crystals of BaFe₂As₂ actually rotates the easy axis of the collinear AF order near T_N/T_s , and such effect due to spin-orbit coupling must be taken into account to unveil the intrinsic electronic/magnetic properties of the system.

Understanding the intrinsic electronic, magnetic, and nematic properties of iron pnictides such as BaFe₂As₂ form the basis to unveil the microscopic origin of high-temperature superconductivity because the system is a parent compound of iron-based superconductors [1–5]. As a function of decreasing temperature, BaFe₂As₂ first exhibits a tetragonal-to-orthorhombic structural transition at T_s and forms a nematic ordered phase, followed closely by a collinear antiferromagnetic (AF) order with moment along the a -axis of the orthorhombic lattice below the Néel temperature T_N ($\leq T_s$) [Fig. 1(a)] [6–9]. Since single crystals of BaFe₂As₂ form twin-domains in the orthorhombic state below T_s , an external uniaxial pressure applied along one-axis of the orthorhombic lattice has been widely used as an effective method to acquire single domains of iron pnictide crystals and determine their intrinsic transport [10–15], electronic [16–18], and magnetic [19–21] properties [inset in Fig. 1(b)]. Although uniaxial pressure necessary to detwin single crystals of BaFe₂As₂ is known to increase T_N [Fig. 1(b)] [22–25] and create in-plane resistivity anisotropy above T_s [14], it is generally assumed that it only induces a small strain on the sample and does not significantly modify the electronic and magnetic properties of the system [10–19, 21]. Recently, nuclear magnetic resonance (NMR) experiments have revealed that an in-plane uniaxial strain on BaFe₂As₂ induces an enhancement of the low-energy spin fluctuations along the c -axis in the paramagnetic state above T_N [26]. However, it is unclear whether the applied uniaxial pressure can actually modify the collinear AF structure of the system [Fig. 1(a)] [6, 7].

In this work, we use polarized neutron scattering and unpolarized neutron diffraction to demonstrate that an in-plane uniaxial pressure necessary to detwin BaFe₂As₂ also induces a c -axis ordered magnetic moment and changes the easy axis of the collinear AF structure around the magnetic/nematic critical scattering temperature regime where the applied pressure has a large impact on the lattice structure of the system [Figs. 1(c-g)] [27]. In addition, we find that the applied pressure induces c -axis polarized critical spin fluctuations that diverge near T_N/T_s , confirming the results of NMR experiments [26]. Therefore, uniaxial pressure on BaFe₂As₂ that breaks the tetragonal lattice symmetry also induces changes in the magnetic easy axis near the critical regime of the AF/nematic phase transitions, indicating that the intrinsic electronic and magnetic properties of the system near T_N/T_s are much different from naive expectations.

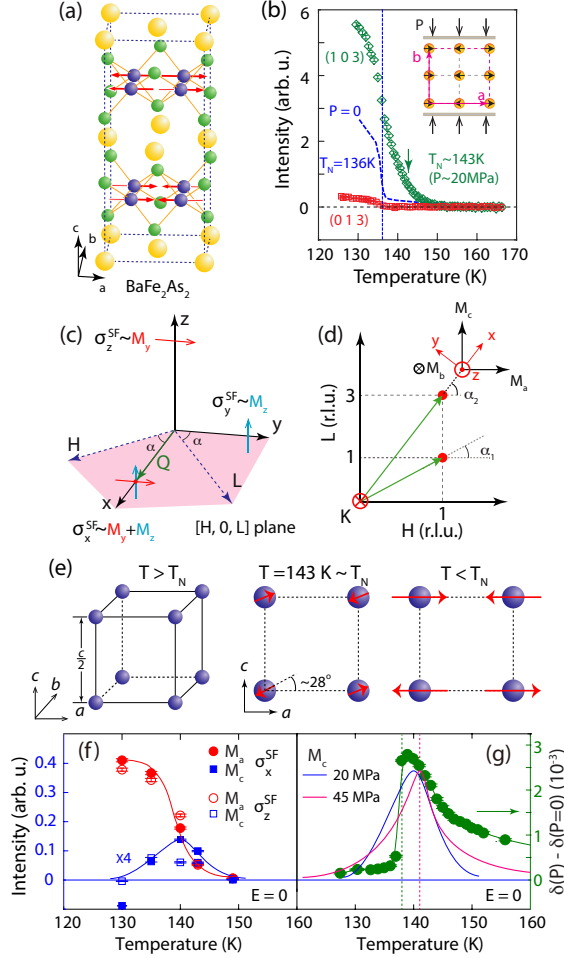


FIG. 1: **Summary of the effect of uniaxial pressure on crystalline lattice and magnetic structures of $\text{Ba}_2\text{Fe}_2\text{As}_2$.** (a) Crystal and AF structure of BaFe_2As_2 . The red arrows indicate the a -axis direction of magnetic moments. (b) Magnetic order parameters measured at $\mathbf{Q}_1 = (1, 0, 3)$ and $(0, 1, 3)$ under uniaxial pressure, revealing $T_N = 143$ K. The blue dashed curve denotes the magnetic order parameter measured on a strain-free sample with $T_N = 136$ K. (c) Scattering geometry of polarized neutron scattering experiment in the $[H, 0, L]$ plane. (d) The reciprocal space, where the fluctuating moments along the a -, b -, and c -axis directions are marked as M_a , M_b , and M_c , respectively. (e) Spin arrangements of BaFe_2As_2 in the paramagnetic (left), near T_N (middle), and low-temperature AF state. (f) Temperature dependence of the static ordered magnetic moment M_a and M_c as determined from $\sigma_{x,z}^{SF}$ at $(1, 0, 1)$ and $(1, 0, 3)$. The vertical error bars are estimated errors from fits-to-order parameters. (g) Comparison of temperature dependence of the strain-induced lattice distortion from Ref. [27] and our estimated M_c at ~ 20 (blue solid line) and ~ 45 (pink solid line) MPa.

RESULTS

Collinear magnetic order in twinned BaFe_2As_2 . Without external uniaxial pressure, BaFe_2As_2 exhibits separate weakly first-order magnetic and second-order structural phase transitions ($T_s > T_N$ by ~ 0.75 K) [7]. The spins within each FeAs layer are collinear and arranged antiferromagnetically along the a -axis and ferromagnetically along the b -axis of orthorhombic structure with lattice parameters of a and b , respectively ($a > b$). Along the out-of-plane direction, spins are arranged antiferromagnetically within one chemical unit cell (lattice parameter c), but have no net magnetic moment along the c -axis [Fig. 1(a)] [6, 7]. For a collinear Ising antiferromagnet with second order (or weakly first order) magnetic phase transition, magnetic critical scattering with moments polarized along the longitudinal (parallel to the ordered moment or a -axis) direction should diverge at T_N , while spin fluctuations with moments polarized transverse to the ordered moment (b - and c -axis) direction should not diverge [28–32]. Unpolarized [33] and polarized [34] neutron scattering experiments on strain-free BaFe_2As_2 confirm this expectation. While the longitudinal component (M_a) of the magnetic critical scattering, defined as low-energy spin fluctuations polarized

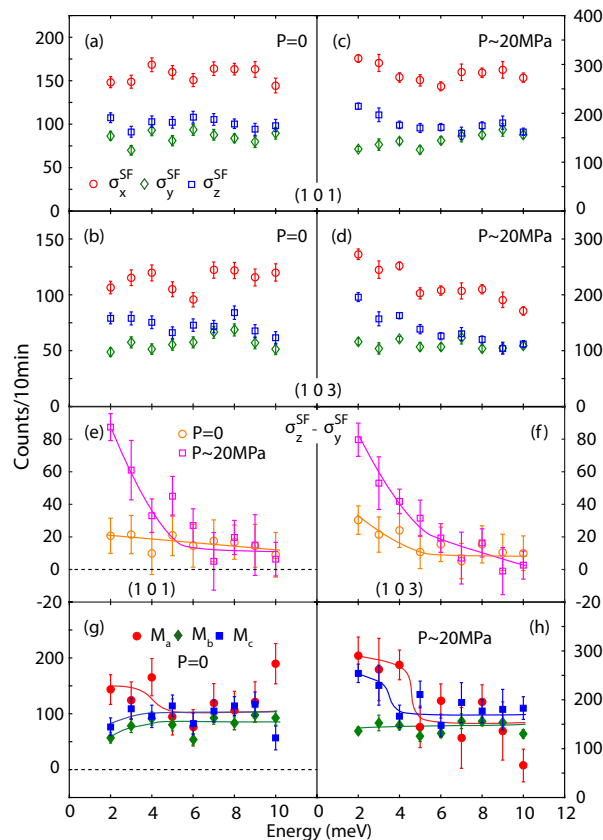


FIG. 2: **The energy dependence of the neutron spin-flip magnetic scattering near T_N without and with uniaxial pressure.** (a-d) Energy scans of σ_x^{SF} (red circle), σ_y^{SF} (green diamond), and σ_z^{SF} (blue square) under (a, b) $P = 0$ and $T = 138$ K [34] and (c, d) ~ 20 MPa and $T = 145$ K at the two AF wave vectors (1, 0, 1) and (1, 0, 3). (e, f) Comparison of $P = 0$ and $P \approx 20$ MPa ($\sigma_z^{SF} - \sigma_y^{SF}$) at (1, 0, 1) and (1, 0, 3). (g, h) Energy dependence of M_a , M_b , and M_c extracted from the raw data in (a-d). The solid lines are guides to the eyes and the error bars represent one standard deviation.

along the a -axis direction, diverges at T_N , the transverse components M_b and M_c along the b and c -axis, respectively [Figs. 1(c,d)], do not diverge at T_N .

Effect of uniaxial pressure on lattice parameters of BaFe_2As_2 . The in-plane uniaxial pressure-induced tetragonal symmetry-breaking lattice distortion [$\delta(P \neq 0) - \delta(P = 0)$, where $\delta = (a - b)/(a + b)$] has a Curie-Weiss temperature dependence in the paramagnetic state and peaks near T_N/T_s , but is greatly suppressed below T_N/T_s when the intrinsic orthorhombic lattice of BaFe_2As_2 sets in [Fig. 1(g)] [27]. In the paramagnetic state, NMR experiments on BaFe_2As_2 suggest that an in-plane uniaxial strain can induce a diverging c -axis polarized spin susceptibility χ_c'' , which equals to M_c in the zero energy limit, on approaching T_N/T_s [26]. Since c -axis polarized low-energy spin fluctuations do not diverge around T_N/T_s in the strain-free BaFe_2As_2 [34], it is important to confirm the NMR results and determine if the diverging χ_c'' is a precursor of a new magnetic order with a component along the c -axis [Fig. 1(f)] [28].

Neutron polarization analysis of spin excitations in detwinned BaFe_2As_2 . Our polarized neutron scattering experiments were carried out on the CEA CRG-IN22 triple-axis spectrometer equipped with Cryopad capability at the Institut Laue Langevin and the BT-7 triple-axis spectrometer at the NIST Center for Neutron Research. The experimental setup for IN22 has been described in detail before [34–39], while polarized neutrons were controlled and analyzed using a polarized ^3He filter on BT-7 [40, 41]. We have also carried out unpolarized neutron diffraction experiments on BT-7 using an in-situ uniaxial pressure device [25]. The wave vector transfer \mathbf{Q} in reciprocal space in \AA^{-1} is defined as $\mathbf{Q} = H\mathbf{a}^* + K\mathbf{b}^* + L\mathbf{c}^*$, with $\mathbf{a}^* = (2\pi/a)\hat{\mathbf{a}}$, $\mathbf{b}^* = (2\pi/b)\hat{\mathbf{b}}$, and $\mathbf{c}^* = (2\pi/c)\hat{\mathbf{c}}$, where $a \approx b \approx 5.6$ \AA , $c = 12.96$ \AA , and H, K, L are Miller indices. In this notation, the collinear AF structure of BaFe_2As_2 in Fig. 1(a) gives magnetic Bragg peaks at $[H, K, L] = [1, 0, L]$ with $L = 1, 3, \dots$. The magnetic responses of the system at a particular \mathbf{Q} along the orthorhombic lattice a -, b -, and c -axis directions are marked as M_a , M_b , and M_c , respectively [Figs. 1(a-d)]. The scattering plane is $[H, 0, L]$. The incident neutrons are polarized along the \mathbf{Q} (x), perpendicular

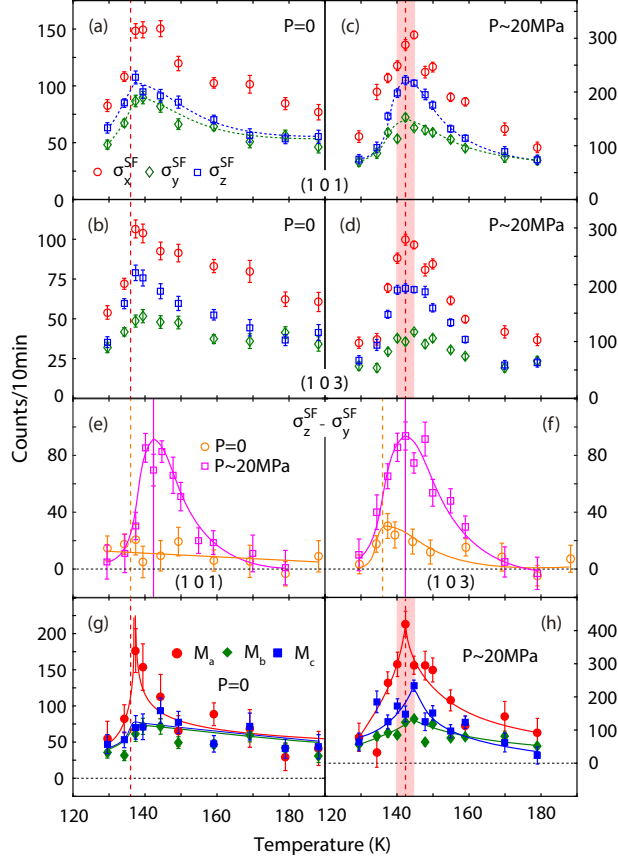


FIG. 3: **Temperature dependence of the magnetic scattering across T_N at $E = 2$ meV without and with uniaxial pressure.** Temperature dependence of σ_x^{SF} , σ_y^{SF} , and σ_z^{SF} at $E = 2$ meV of (a, b) uniaxial pressure-free [34] and (c, d) pressured ($P \approx 20$ MPa) BaFe_2As_2 at (a, c) (1,0,1) and (b, d) (1,0,3). (e, f) Comparison of $P = 0$ and $P \approx 20$ MPa ($\sigma_z^{SF} - \sigma_y^{SF}$) at (1,0,1) and (1,0,3). (g, h) Temperature dependence of M_a , M_b , and M_c at $E = 2$ meV for (g) uniaxial pressure-free and (h) pressured sample estimated from the data in (a-d). The dotted and solid lines are guides to the eye and the error bars represent one standard deviation. The vertical dashed and solid lines mark T_N/T_s at $P = 0$ and $P \approx 20$ MPa, respectively.

to \mathbf{Q} but in the scattering plane (y), and perpendicular to both \mathbf{Q} and the scattering plane (z) [Fig. 1(c)]. In this geometry, the neutron spin-flip (SF) scattering cross sections σ_x^{SF} , σ_y^{SF} , and σ_z^{SF} are related to the components M_a , M_b , and M_c via $\sigma_x^{SF} = \frac{R}{R+1}M_y + \frac{R}{R+1}M_z + B$, $\sigma_y^{SF} = \frac{1}{R+1}M_y + \frac{R}{R+1}M_z + B$, and $\sigma_z^{SF} = \frac{R}{R+1}M_y + \frac{1}{R+1}M_z + B$, where R is the flipping ratio ($R = \sigma_{\text{Bragg}}^{NSF}/\sigma_{\text{Bragg}}^{SF} \approx 13$), B is the background scattering, $M_y = \sin^2 \alpha M_a + \cos^2 \alpha M_c$ with α being the angle between $[H, 0, 0]$ and \mathbf{Q} , and $M_z = M_b$ [Fig. 1(d)] [34–39].

Figure 1(b) compares the temperature dependencies of the (1,0,3) magnetic Bragg peak for strain-free and strained BaFe_2As_2 . At zero external pressure ($P = 0$ and strain-free), the magnetic scattering shows an order parameter like increase below $T_N = 136$ K [34]. When an uniaxial pressure of $P \approx 20$ MPa is applied along the b -axis of BaFe_2As_2 , the Néel temperature of the sample increases to $T_N = 143$ K [25]. The vanishingly small magnetic scattering intensity at $\mathbf{Q} = (0, 1, 3)$ suggests that the sample is essentially $\sim 100\%$ detwinned [Fig. 1(b)].

Figures 2(a) and 2(b) show the energy dependence of σ_x^{SF} , σ_y^{SF} , and σ_z^{SF} in the zero pressure paramagnetic state at $T \approx 1.015T_N \approx 138$ K for magnetic positions (1,0,1) and (1,0,3) [34]. Figures 2(c) and 2(d) show identical scans as those of Figs. 2(a) and 2(b), respectively, in the paramagnetic state at $T \approx 1.014T_N \approx 145$ K with uniaxial pressure of $P \approx 20$ MPa. Comparison of the Figs. 2(a) and 2(c) reveals that σ_z^{SF} is clearly larger than σ_y^{SF} below ~ 5 meV in the uniaxial strained sample. Since the (1,0,1) peak corresponds to $\alpha_1 = 23.4^\circ$ giving $M_y \approx 0.16M_a + 0.84M_c$ [Fig. 1(d)] [34], the increased σ_z^{SF} in strained BaFe_2As_2 is mostly due to the increased M_c . For the (1,0,3) peak, which corresponds to $\alpha_2 = 52.4^\circ$, $M_y \approx 0.63M_a + 0.37M_c$, and the scattering is therefore much less sensitive to strain-induced changes in M_c . To conclusively determine the effect of uniaxial pressure on M_c , we consider $\sigma_z^{SF} - \sigma_y^{SF} \propto M_y - M_b$. Since M_b (or σ_y^{SF}) does not diverge at T_N or change as a function of uniaxial pressure as seen in NMR [26] and neutron

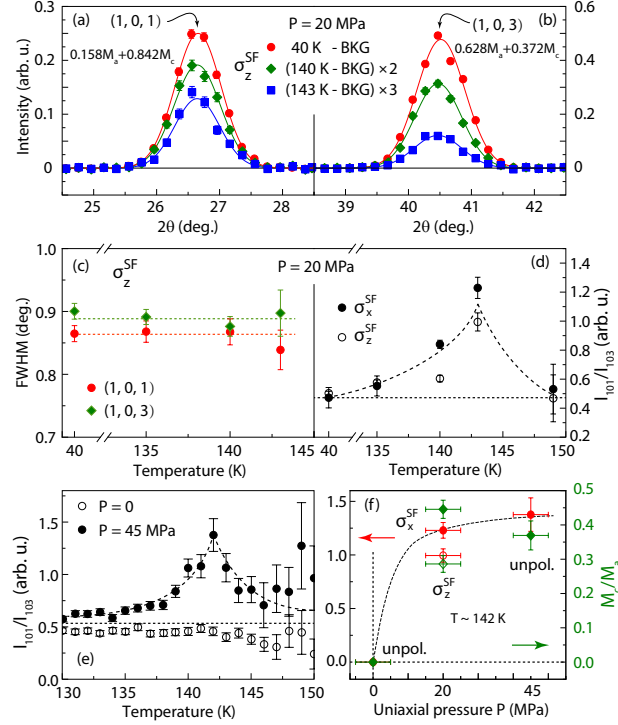


FIG. 4: **Uniaxial pressure dependence of the magnetic order and correlations.** Elastic $\theta/2\theta$ scans of σ_z^{SF} across (a) (1,0,1) and (b) (1,0,3) at different temperatures and $P = 20$ MPa. The data are collected on BT-7 using final neutron energy of 14.7 meV with instrumental energy resolution of about 1.3 meV. Similar scans of σ_z^{SF} are discussed in [42]. σ_y^{SF} was unavailable at the time of this experiment. (c) FWHM of the elastic (1,0,1) and (1,0,3) scans across T_N/T_s . (d) Temperature dependence of $I_{101}/I_{103} \propto (0.16M_a + 0.84M_c)/(0.63M_a + 0.37M_c)$. (e) Temperature dependence of I_{101}/I_{103} at $P \approx 0$ and ~ 45 MPa uniaxial pressure obtained using in-situ uniaxial pressure device with unpolarized neutrons on BT-7. (f) Pressure dependence of I_{101}/I_{103} (red symbols, left axis) and M_c/M_a (green symbols, right axis) at $T \sim 142$ K. The data points for $P = 0$ and 45 MPa were measured with unpolarized neutron scattering. The data points for $P = 20$ MPa were measured with polarized mode with the open (solid) symbols obtained from σ_z^{SF} (σ_x^{SF}). The black dashed curve is a guide to the eye for the data points. unpol. denotes unpolarized neutron scattering measurements. The vertical error bars in (a,b,d,e) represent statistical errors of 1 standard deviation. The error bars in (c) are estimated errors from fits to magnetic Bragg peak widths. The error bars in (f) are our estimated errors from fits to magnetic order parameters and applied uniaxial pressure.

polarization analysis [Figs. 2(a-d)], the effect of uniaxial pressure can be seen directly from the energy dependence of $\sigma_z^{SF} - \sigma_y^{SF}$ at the (1,0,1) [Fig. 2(e)] and (1,0,3) [Fig. 2(f)]. Without uniaxial pressure, $\sigma_z^{SF} - \sigma_y^{SF}$ does not diverge at the (1,0,1) position but diverges at (1,0,3) at low energies consistent with the expectation that spin fluctuations at (1,0,1) is mostly probing M_c . With uniaxial pressure, we see clear divergence of low-energy spin fluctuations at (1,0,1) below ~ 5 meV, thus unambiguously confirming the uniaxial pressure induced M_c enhancement around T_N observed in NMR experiments [26]. To further clarify the energy dependence of M_a , M_b , and M_c , we estimate these components from measurements at the (1,0,1) and (1,0,3) positions as described in Ref. [34]. By comparing the energy dependence of M_a , M_b , and M_c in strain-free [Fig. 2(g)] and strained [Fig. 2(h)] BaFe₂As₂, we again see that the effect of uniaxial strain is to enhance M_c below about 4 meV, consistent with the NMR measurements which probe M_c or χ_c'' in the zero energy limit [26].

To demonstrate further the effect of uniaxial strain on the magnetic critical scattering of BaFe₂As₂, we show in Fig. 3 the temperature dependence of σ_x^{SF} , σ_y^{SF} , and σ_z^{SF} at $E = 2$ meV for the strain-free [Figs. 3(a,b)] [34] and strained [Figs. 3(c,d)] samples. At $\mathbf{Q} = (1,0,1)$, uniaxial strain clearly enhances σ_z^{SF} around T_N/T_s , where $\sigma_z^{SF} \approx M_y \approx 0.16M_a + 0.84M_c$, again consistent with the strain enhanced χ_c'' in the NMR measurements [26]. Figures 3(b) and 3(d) show similar measurements at $\mathbf{Q} = (1,0,3)$, which reveal much less enhancement of σ_z^{SF} because $\sigma_z^{SF} \approx M_y \approx 0.63M_a + 0.37M_c$. Figure 3(e) shows temperature dependence of $\sigma_z^{SF} - \sigma_y^{SF}$ across T_N at the (1,0,1) peak without and with uniaxial pressure. Since spin fluctuations at the (1,0,1) position is mostly sensitive to M_c , we see no divergence across T_N in zero pressure case. Upon application of a ~ 20 MPa uniaxial pressure, the scattering clearly reveals a diverging behavior at the pressured enhanced T_N (solid vertical line) [Fig. 3(e)]. Similar

measurements at the $(1, 0, 3)$ position, which is more sensitive to M_a , show diverging magnetic scattering at T_N with and without uniaxial pressure consistent with the NMR results [Fig. 3(f)] [26]. Figures 3(g) and 3(h) show the temperature dependencies of the estimated M_a , M_b , and M_c for strain-free and strained BaFe₂As₂, respectively, using the data in Figs. 3(a-d). Comparing with the normal behavior of the strain-free BaFe₂As₂ [Fig. 3(g)], the M_c in strained BaFe₂As₂ clearly diverges around T_N/T_s [Fig. 3(h)], although the error bars of the data became worst after the data manipulation [42].

Effect of uniaxial pressure on static AF order of BaFe₂As₂. In principle, a diverging dynamic spin susceptibility in the paramagnetic state of a system is an indication of the eventual magnetic order below T_N [28–32]. For strain-free BaFe₂As₂, the magnetic ordered moment is along the a -axis with no net moment along the b -axis and c -axis directions [6, 7]. Therefore, only the M_a component of the spin susceptibility diverges at T_N [Figs. 3(e,f,g)] [34]. The observation of a diverging M_c in strained BaFe₂As₂, in addition to the usual diverging M_a [Figs. 3(e,f,h)], suggests that the applied strain may induce static magnetic ordered moment along the c -axis. To test this hypothesis, we carried out polarized neutron diffraction measurements on BaFe₂As₂ as a function of uniaxial pressure, focusing on the temperature and neutron polarization dependence of the scattering at $\mathbf{Q} = (1, 0, L)$ with $L = 0, 1, 2, 3$, and 5. At wave vectors $(1, 0, 0)$ and $(1, 0, 2)$, there is no evidence of magnetic scattering, consistent with uniaxial pressure-free BaFe₂As₂ [42].

Figures 4(a) and 4(b) show $\theta/2\theta$ scans of σ_z^{SF} around $(1, 0, 1)$ and $(1, 0, 3)$, respectively, at different temperatures. Since σ_z^{SF} at these two wave vectors probes different combinations of M_a and M_c , one can obtain magnitudes of the static ordered moments along the a -axis and c -axis directions at these temperatures. Figure 4(c) shows the temperature dependencies of the full-width-at-half-maximum (FWHM) of these peaks, indicating that the spin-spin correlation lengths are instrumental resolution limited and temperature independent. Figure 4(d) plots the magnetic scattering intensity ratio between $(1, 0, 1)$ (I_{101}) and $(1, 0, 3)$ (I_{103}), which measures the relative strength of M_c and reveals a clear peak around T_N/T_s .

To further determine the effect of uniaxial pressure on c -axis ordered moment and its pressure dependence, we carried out unpolarized neutron diffraction measurements focusing on the magnetic scattering intensity ratio between $(1, 0, 1)$ (I_{101}) and $(1, 0, 3)$ (I_{103}) using an in-situ uniaxial pressure device. Since our polarized neutron diffraction measurements revealed no ordered moment M_b , we used unpolarized neutron diffraction on BT-7 to improve the statistics of the data across T_N . Figure 4(e) compares the measured I_{101}/I_{103} from 130 K to 150 K at $P \approx 0$ and 45 MPa uniaxial pressure. Consistent with earlier work [6, 7], I_{101}/I_{103} is approximately temperature independent across T_N at $P \approx 0$, thus indicating that the internal strain of the system does not induce a c -axis ordered moment. Upon applying an uniaxial pressure of $P \approx 45$ MPa, the identical measurement shows a dramatic peak at T_N , thus confirming the results of Figs. 4(a-d). Figure 4(f) shows the uniaxial pressure dependence of the measured M_c/M_a at T_N , suggesting that the ordered c -axis moment saturates with increasing pressure above 45 MPa.

Figure 1(f) shows the temperature dependencies of the magnetically ordered moments along the a -axis (M_a) and c -axis (M_c) directions obtained by comparing σ_x^{SF} and σ_z^{SF} at wave vectors $(1, 0, 1)$ and $(1, 0, 3)$ [42]. In the low temperature AF ordered state, the strain-free and strained BaFe₂As₂ have the standard collinear AF structure with no evidence of M_c [right panel in Fig. 1(e) and Fig. 4(e)] [6, 7]. On warming to 143 K just below T_N , the easy-axis tilts from the a -axis towards the c -axis with an angle of $\sim 28^\circ$ [middle panel in Fig. 1(e)]. Finally, on warming to temperatures well above T_N , there is no static AF order [left panel in Fig. 1(e)]. Figure 1(g) shows the temperature dependence of M_c at ~ 20 (blue solid line) and ~ 45 (pink solid line) MPa uniaxial pressure, compared with the uniaxial strain-induced lattice distortion $\delta(P \approx 20 \text{ MPa}) - \delta(P = 0)$ (green solid circles and lines) obtained from neutron Larmor diffraction experiments [27]. The similarity of the data suggests that the c -axis aligned magnetic moment arises from the uniaxial pressure-induced lattice distortion.

DISCUSSION

Theoretically, the in-plane electronic anisotropy of the iron pnictides is expected to couple linearly to the lattice orthorhombicity by the Ginzburg-Landau free-energy formalism if one ignores the effect of spin-orbit coupling induced magnetic anisotropy [9, 27]. From this perspective, in-plane uniaxial strain should only induce in-plane electronic anisotropy. The discovery of a c -axis ordered magnetic moment coupled exclusively with uniaxial pressure-induced lattice distortion suggests that such an effect cannot be only associated with the lattice orthorhombicity of the system, as M_c becomes vanishingly small in the low-temperature orthorhombic phase with large in-plane lattice distortion. This is also different from the c -axis moment AF structure in Ba_{1-x}K_xFe₂As₂ in the sense that the c -axis order appears exclusively in the tetragonal phase [43, 44], while the c -axis moment appears in BaFe₂As₂ only near the peak of the nematic susceptibility around T_N/T_s . Although there is currently no theoretical understanding of this

observation, it must arise from spin-orbit coupling induced magnetic anisotropy [45]. Our discovery opens a new avenue to control magnetic order in nematic materials using mechanical strain instead of magnetic fields. The strong coupling of the c -axis aligned magnetic order with an in-plane pressure-induced lattice distortion offers the potential for the next generation of mechanical-strain-controlled magnetic switches. One must consider the presence of the magnetically ordered moment along the c -axis in mechanically detwinned iron pnictides in order to understand their intrinsic electronic, magnetic, and nematic properties.

Alternatively, our observations are also consistent with strain inducing a proximate XY spin anisotropy near T_N/T_s . In this scenario, while a -axis is energetically favorable in terms of spin anisotropy, c -axis is very close. This allows for a distribution of large (resolution-limited but not long-ranged ordered) and long-lived (quasi-static) collinear magnetic domains, with their collinear spin direction in the ac -plane. The ratio between I_{101}/I_{103} [Figs. 4(d,e)] is then a measure of the distribution, reflective of the difference in spin anisotropy energies along the a - and c -axis. Similar to when the easy axis tilts from a -axis towards c -axis under strain [Fig. 1(e)], the change to a proximate XY spin anisotropy under strain also indicates of a large and highly unusual effect of strain on the spin anisotropy.

In conclusion, we have used polarized and unpolarized neutron scattering to study the magnetic structure and critical scattering in uniaxial strained BaFe_2As_2 . We find that the uniaxial pressure necessary to make single domain samples of BaFe_2As_2 also induces c -axis polarized critical magnetic scattering and static magnetic order around T_N/T_s . The size of the c -axis ordered moment is associated with the uniaxial pressure-induced lattice distortion, instead of the lattice orthorhombicity. These results indicate that in addition to detwining BaFe_2As_2 , uniaxial pressure applied on the sample actually modifies the magnetic structure of the system. Therefore, infrared [46], angle resolved photoemission [16], and Raman spectroscopy [47, 48] experiments on mechanically detwinned BaFe_2As_2 near the magnetic and nematic phases should be re-examined to take into account the effect of strain-induced change to the spin anisotropy on the in-plane electronic and magnetic properties.

METHODS

Sample preparation and experimental details. BaFe_2As_2 single crystals were grown by the self-flux method using the same growth procedure as described before [19]. Our polarized inelastic neutron scattering experiments were carried out using the IN22 CEA-CRG triple-axis spectrometer at the Institut Laue-Langevin, Grenoble, France [49]. Polarized neutrons were produced using a focusing Heusler monochromator and analyzed with a focusing Heusler analyzer with a final wave vector of $k_f = 2.662 \text{ \AA}^{-1}$. The experimental setups for uniaxial pressured and pressure freed experiments are identical. However, it is difficult to directly compare the scattering intensity of these two experiments since the sample masses, their relative positions in the beam, and background scattering of these two experiments are different. Nevertheless, one can safely compare the relative intensity changes of these two experiments. The polarized elastic neutron scattering experiments were carried out on BT-7 utilizing ^3He polarizers immediately before and after the sample at NIST center for neutron research, Gaithersburg, Maryland, USA [40, 41]. The unpolarized neutron diffraction experiments in Fig. 4(e) were carried out using a pyrolytic graphite monochromator and analyzer with pyrolytic graphite filter in the beam. Experiments on twinned BaFe_2As_2 without external uniaxial pressure were performed on ~ 12 -g aligned single crystals as described before [34]. The polarized inelastic neutron scattering experiments on uniaxial pressured detwinned BaFe_2As_2 were performed using 12 pieces cut single crystals (~ 3 -g, Fig. S1) [21]. The BT-7 measurements were carried out on a single piece of BaFe_2As_2 mounted on a newly built in-situ uniaxial pressure device and the neutron wave vectors are set at $k_i = k_f = 2.662 \text{ \AA}^{-1}$.

Determination of \mathbf{M}_a , \mathbf{M}_b and \mathbf{M}_c . In our previous polarized neutron scattering studies of iron pnictides, we have established the method for determining the spin-fluctuation components M_β ($\beta = a, b, c$) along the lattice axes via comparing the spin-flip scattering σ_γ^{SF} ($\gamma = x, y, z$) at two equivalent magnetic wave vectors (such as $\mathbf{Q}_1 = (1, 0, 1)$ and $\mathbf{Q}_2 = (1, 0, 3)$ as shown in Fig. 1 of the main text). The definition of the directions x, y and z are described in Fig. 1. σ_γ^{SF} is directly related to the spin-fluctuation components by:

$$\begin{cases} \sigma_x^{\text{SF}}(\mathbf{Q}) = F^2(\mathbf{Q}) \sin^2 \alpha_{\mathbf{Q}} \frac{R}{R+1} M_a + F^2(\mathbf{Q}) \frac{R}{R+1} M_b + F^2(\mathbf{Q}) \cos^2 \alpha_{\mathbf{Q}} \frac{R}{R+1} M_c + B(\mathbf{Q}), \\ \sigma_y^{\text{SF}}(\mathbf{Q}) = F^2(\mathbf{Q}) \sin^2 \alpha_{\mathbf{Q}} \frac{1}{R+1} M_a + F^2(\mathbf{Q}) \frac{R}{R+1} M_b + F^2(\mathbf{Q}) \cos^2 \alpha_{\mathbf{Q}} \frac{1}{R+1} M_c + B(\mathbf{Q}), \\ \sigma_z^{\text{SF}}(\mathbf{Q}) = F^2(\mathbf{Q}) \sin^2 \alpha_{\mathbf{Q}} \frac{R}{R+1} M_a + F^2(\mathbf{Q}) \frac{1}{R+1} M_b + F^2(\mathbf{Q}) \cos^2 \alpha_{\mathbf{Q}} \frac{R}{R+1} M_c + B(\mathbf{Q}) \end{cases} \quad (1)$$

where α is the angle between $(1, 0, 0)$ and \mathbf{Q} (Fig. 1), $F(\mathbf{Q})$ is magnetic form factor of Fe^{2+} , R is the flipping ratio ($R = \sigma_{\text{Bragg}}^{NSF} / \sigma_{\text{Bragg}}^{SF} \approx 13$), and B is the polarization-independent background scattering.

From Eq. (1), we can get four equations for our results on \mathbf{Q}_1 and \mathbf{Q}_2 :

$$\left\{ \begin{array}{l} \sigma_x^{\text{SF}}(\mathbf{Q}_1) - \sigma_y^{\text{SF}}(\mathbf{Q}_1) = \frac{R-1}{R+1} F^2(\mathbf{Q}_1) [\sin^2 \alpha_1 M_a + \cos^2 \alpha_1 M_c], \\ \sigma_x^{\text{SF}}(\mathbf{Q}_2) - \sigma_y^{\text{SF}}(\mathbf{Q}_2) = r \frac{R-1}{R+1} F^2(\mathbf{Q}_2) [\sin^2 \alpha_2 M_a + \cos^2 \alpha_2 M_c], \\ \sigma_x^{\text{SF}}(\mathbf{Q}_1) - \sigma_z^{\text{SF}}(\mathbf{Q}_1) = \frac{R-1}{R+1} F^2(\mathbf{Q}_1) M_b, \\ \sigma_x^{\text{SF}}(\mathbf{Q}_2) - \sigma_z^{\text{SF}}(\mathbf{Q}_2) = r \frac{R-1}{R+1} F^2(\mathbf{Q}_2) M_b, \end{array} \right. \quad (2)$$

in which r is the intensity ratio factor between \mathbf{Q}_1 and \mathbf{Q}_2 to account for the differences in sample illumination volume and the convolution with instrumental resolution. The third and fourth equations in Eq. (2) can be used to determine the ratio r and M_b , and the first two equations for M_a and M_c . More details concerning the determination of the spin-fluctuation components M_a , M_b and M_c can be find elsewhere [39]. Although this method can determine the values of M_a , M_b and M_c , it also results in large error bars of their values. To more accurately determine the effect of uniaxial pressure on M_a and M_c , we consider the differences between $\sigma_z^{\text{SF}}(\mathbf{Q}) - \sigma_y^{\text{SF}}(\mathbf{Q})$ at \mathbf{Q}_1 and \mathbf{Q}_2 .

$$\left\{ \begin{array}{l} \sigma_z^{\text{SF}}(\mathbf{Q}_1) - \sigma_y^{\text{SF}}(\mathbf{Q}_1) = \frac{R-1}{R+1} F^2(\mathbf{Q}_1) [\sin^2 \alpha_1 M_a + \cos^2 \alpha_1 M_c - M_b] \propto 0.16 M_a + 0.84 M_c - M_b, \\ \sigma_z^{\text{SF}}(\mathbf{Q}_2) - \sigma_y^{\text{SF}}(\mathbf{Q}_2) = r \frac{R-1}{R+1} F^2(\mathbf{Q}_2) [\sin^2 \alpha_2 M_a + \cos^2 \alpha_2 M_c - M_b] \propto 0.63 M_a + 0.37 M_c - M_b, \end{array} \right. \quad (3)$$

As M_b does not diverge in uniaxial pressured and pressure-free cases [26], a comparison of $\sigma_z^{\text{SF}}(\mathbf{Q}_1) - \sigma_y^{\text{SF}}(\mathbf{Q}_1)$ raw data should be most sensitive to changes in M_c , while $\sigma_z^{\text{SF}}(\mathbf{Q}_2) - \sigma_y^{\text{SF}}(\mathbf{Q}_2)$ should be sensitive to changes in both M_a and M_c . The outcome of this analysis is shown in Figs. 2(e,f), 3(e,f).

In our polarized neutron diffraction experiment at BT-7, we have only measured σ_x^{SF} and σ_z^{SF} . In elastic channel, M_β is proportional to the square of the ordered moment (m_β). The determination of M_β follows the same method as described in Eqs. (1) and (2). But we need to apply the Lorentz factor ($L = \frac{1}{\sin 2\theta}$) as we use the integrated intensity of $\theta - 2\theta$ scan to calculate M_β [50], where 2θ is the scattering angle for \mathbf{Q} . Moreover, since no divergence of critical spin fluctuations were observed along the b axis, we can assume the absence of static ordered moment ($M_b = 0$) (even if we consider that quasi-elastic spin fluctuations along b axis within the energy resolution of the elastic scattering could be included in σ_x^{SF} and σ_z^{SF} , it can be neglected at least in σ_z^{SF} because of the small pre-factor $\frac{1}{R+1} \approx 0.07$ before M_b). Then Eq. (2) can be written as:

$$\left\{ \begin{array}{l} \sigma_x^{\text{SF}}(\mathbf{Q}_1) = \sigma_z^{\text{SF}}(\mathbf{Q}_1) = \frac{1}{\sin 2\theta_1} \frac{R}{R+1} F^2(\mathbf{Q}_1) [\sin^2 \alpha_1 M_a + \cos^2 \alpha_1 M_c], \\ \sigma_x^{\text{SF}}(\mathbf{Q}_2) = \sigma_z^{\text{SF}}(\mathbf{Q}_2) = r \frac{1}{\sin 2\theta_2} \frac{R}{R+1} F^2(\mathbf{Q}_2) [\sin^2 \alpha_2 M_a + \cos^2 \alpha_2 M_c], \end{array} \right. \quad (4)$$

Given the magnetic moment is polarized along a axis at $40\text{K} \ll T_N$ with $m_a \approx 0.87 \mu_B$, we can get r , solve M_a and M_c from both σ_x^{SF} and σ_z^{SF} , and determine the magnitude of the c -axis moment induced by uniaxial strain. Taking $m_a = 0.87 \mu_B$ at 40 K, we can get m_a and m_c at other temperatures using the data points shown in Fig. 1(f). From σ_z^{SF} , we get $m_a \approx 0.23 \pm 0.05 \mu_B$ and $m_c \approx 0.12 \pm 0.03 \mu_B$ at 143K, resulting in a canting angle of $\sim 28^\circ$ at this critical temperature. The calculated canting angles are estimated to be about 14° at 140 K and 149 K, and gradually decreases to zero below 135K.

$\sigma_{x,y,z}^{\text{SF}}$ and $M_{a,b,c}$ below and well above T_N at the AF ordering wave vectors. Fig. S2 shows the results of $\sigma_\gamma^{\text{SF}}$ ($\gamma = x, y, z$) below and well above T_N under zero and $P \sim 20$ MPa. At $T = 135$ K ($< T_N$), $\sigma_\gamma^{\text{SF}}$'s for uniaxial pressure-free and pressured cases are shown in Figs. S2(a-d). A comparison of $\sigma_z^{\text{SF}}(\mathbf{Q}_1) - \sigma_y^{\text{SF}}(\mathbf{Q}_1)$ scattering at $P = 0$ and ~ 20 MPa in Fig. S2(e) suggests that the applied uniaxial pressure may enhance M_c around ~ 8 meV. Similar data at \mathbf{Q}_2 in Fig. S2(f) suggest that the effect of uniaxial pressure is limited on M_a at this temperature. Figs. S2(g,h) shows as the converted M_a, M_b and M_c at $T = 135$ K. At $T < T_N$, the data with $P \sim 20$ MPa is qualitatively consistent with that measured on the $P = 0$ sample, except that both the M_a and M_b are gapped below $E > 10$ meV and ~ 6 meV, respectively, while only M_a is gapped below 6 meV for the $P = 0$ sample. Note T_N is $\sim 136\text{K}$ for $P = 0$ and ~ 143 K for $P \sim 20$ MPa. In relative temperature T/T_N , 135K is much lower in the $P \sim 20$ MPa sample ($0.94T_N$) than that in free-standing sample ($0.99T_N$), thus the spin fluctuations are further gapped. For temperatures well above T_N [Figs. S2(i-p)], spin-flip scattering becomes very weak and no qualitative difference were observed for $P = 0$ and $P \sim 20$ MPa.

Comparison of M_β at $\mathbf{Q}=(1, 0)$ and $(0, 1)$. To determine if the uniaxial pressure induced M_c at the AF wave vector $\mathbf{Q} = (1, 0)$ is compensated by magnetic scattering reduction at $(0, 1)$, we compare σ_γ^{SF} between $\mathbf{Q} = (1, 0, L)$ and $(0, 1, L)$ ($L = 1, 3$) at $T = 145$ K [Fig. S3(a-d)]. Figures S3(e) and (f) show the energy dependence of $\sigma_z^{SF}(\mathbf{Q}) - \sigma_y^{SF}(\mathbf{Q})$ at $\mathbf{Q} = (1, 0, 1)/(0, 1, 1)$ and $\mathbf{Q} = (1, 0, 3)/(0, 1, 3)$, respectively. Compared with clear magnetic intensity gains below ~ 6 meV at the AF wave vectors $\mathbf{Q}_1 = (1, 0, 1)$ and $\mathbf{Q}_2 = (1, 0, 3)$, paramagnetic scattering at $\mathbf{Q} = (0, 1, 1)$ and $(0, 1, 3)$ is isotropic in spin space as illustrated by the zero values of $\sigma_z^{SF}(\mathbf{Q}) - \sigma_y^{SF}(\mathbf{Q})$ at these wave vectors. Figures S3(g) and (h) show the energy dependence of M_a , M_b , and M_c extracted from Figs. S3(a-d) at the wave vectors $(1, 0)$ and $(0, 1)$, respectively. Therefore, the applied uniaxial pressure clearly has an impact on magnetic excitations at $(1, 0)$ but has no observable effect at $(0, 1)$, which has weak and featureless energy dependence of isotropic M_a , M_b and M_c [Fig. S3(h)].

Consistent with the weak scattering at $(0, 1, L)$ observed at 145K, temperature dependence of M_a , M_b and M_c at $\mathbf{Q} = (0, 1)$ is much weaker than that at $(1, 0, L)$ and decreases in intensity at T_N (Fig. S4), consistent with the temperature dependence of $(0, 1, 1)$ in detwinned BaFe_2As_2 measured with unpolarized neutron scattering [21].

Uniaxial pressure dependence of the magnetic order and correlations. Fig. S5 summarizes the elastic $\theta - 2\theta$ scans of σ_x^{SF} across $\mathbf{Q} = (1, 0, L)$ ($L = 1, 2, 3$). Similar to the $\theta - 2\theta$ scans of σ_z^{SF} as described in Fig. 4 of the main text, the scans for σ_x^{SF} [Fig. S5(a) and S5(b)] exhibits temperature-independent full-width-at-half-maximum (FWHM) from 40 to 143K [Fig. S5(c)], indicating that the spin-spin correlation length are resolution limited even in the temperature range above $T_N \sim 136$ K of unstrained sample. Fig. S5(d) plots the ratio between the scattering intensity at $(1, 0, 1)$ and $(1, 0, 3)$ (I_{101}/I_{103}), which is greatly enhanced close to T_N . Since $\sigma_x^{SF} = 0.16M_a + 0.84M_c$ at $\mathbf{Q} = (1, 0, 1)$ and $0.37M_a + 0.37M_c$ at $(1, 0, 3)$, the enhancement of I_{101}/I_{103} is consistent with the emergence of a c -axis magnetic moment induced by uniaxial strain. At temperature where M_c is not induced, the ratio $I_{101}/I_{103} = 0.16M_a/0.63M_a \times \frac{\sin^2 2\theta_2}{\sin^2 2\theta_1} \approx 0.5$ (black dashed line in Fig. S5(d), where $\frac{\sin^2 2\theta_2}{\sin^2 2\theta_1}$ accounts for the Lorentz factor. The data points of I_{101}/I_{103} in Fig. S5(d) show that M_c is absent at 149K and below 135K but reaches a maximum at 143K close to T_N . The unpolarized data in Fig. 4(f) shows similar behavior.

In addition to the emergence of M_c , it is also important to understand whether M_c forms a new periodicity along c -axis. The magnetic structure factor of the three-dimensional antiferromagnetic order of BaFe_2As_2 ($\mathbf{k} = (1, 0, 1)$) results in magnetic peaks at $(1, 0, L)$ with $L = 1, 3, 5\dots$ and the absence of magnetic scattering at $(1, 0, L)$ with $L = 0, 2, 4\dots$. If the induced M_c forms a larger magnetic unit cell along c axis that ensures the presence of $(1, 0, 1)$ and $(1, 0, 3)$, one can expect detectable magnetic scattering at $L=0, 2$. However, the three-point $\theta - 2\theta$ across $(1, 0, 2)$ in Fig. S5 shows that the intensity for $(1, 0, 2)$ is smaller than $1/3000$ of $(1, 0, 3)$, which rules out this possibility and further confirm our conclusion about the canting-moment picture as shown in Fig. 1 of the main text.

Data availability. The data that support the findings of this study are available from the corresponding authors on request, and will be available at [49].

* These authors made equal contributions to this work.

† Electronic address: luxy@bnu.edu.cn

‡ Electronic address: pdai@rice.edu

- [1] H. Hosono and K. Kuroki, *Physica C*, **514**, 399 (2015).
- [2] D. C. Johnston, *Adv. Phys.* **59**, 803 (2010).
- [3] G. R. Stewart, *Rev. Mod. Phys.* **83**, 1589 (2011).
- [4] D. J. Scalapino, *Rev. Mod. Phys.* **84**, 1383 (2012).
- [5] P. C. Dai, *Rev. Mod. Phys.* **87**, 855 (2015).
- [6] Q. Huang, Y. Qiu, Wei Bao, M. A. Green, J. W. Lynn, Y. C. Gasparovic, T. Wu, G. Wu, X. H. Chen, *Phys. Rev. Lett.* **101**, 257003 (2008).
- [7] M. G. Kim, R. M. Fernandes, A. Kreyssig, J. W. Kim, A. Thaler, S. L. Bud'ko, P. C. Canfield, R. J. McQueeney, J. Schmalian, A. I. Goldman, *Phys. Rev. B* **83**, 134522 (2011).
- [8] R. M. Fernandes, A. V. Chubukov, J. Schmalian, *Nat. Phys.* **10**, 97 (2014).
- [9] A. E. Böhmer, C. Meingast, C. R. Physique **17** 90 (2016).
- [10] I. R. Fisher, L. Degiorgi, and Z. X. Shen, *Rep. Prog. Phys.* **74**, 124506 (2011).
- [11] J.-H. Chu, J. G. Analytis, K. De Greve, P. L. McMahon, Z. Islam, Y. Yamamoto, and I. R. Fisher, *Science* **329**, 824 (2010).
- [12] J.-H. Chu, H.-H. Kuo, J. G. Analytis, and I. R. Fisher, *Science* **337**, 710 (2012).
- [13] M. A. Tanatar, E. C. Blomberg, A. Kreyssig, M. G. Kim, N. Ni, A. Thaler, S. L. Bud'ko, P. C. Canfield, A. I. Goldman, I. I. Mazin, and R. Prozorov, *Phys. Rev. B* **81**, 184508 (2010).
- [14] Haoran Man, Xingye Lu, Justin S. Chen, Rui Zhang, Wenliang Zhang, Huiqian Luo, J. Kulda, A. Ivanov, T. Keller, Emilia

- Morosan, Qimiao Si, and Pengcheng Dai, Phys. Rev. B **92**, 134521 (2015).
- [15] David W. Tam, Weiyi Wang, Li Zhang, Yu Song, Rui Zhang, Scott V. Carr, H. C. Walker, Toby G. Perring, D. T. Adroja, and Pengcheng Dai, Phys. Rev. B **99**, 134519 (2019).
- [16] M. Yi, Y. Zhang, Z.-X. Shen, and D. H. Lu, npj Quantum Materials, **2**, 57 (2017).
- [17] H. Pfau, C. R. Rotundu, J. C. Palmstrom, S. D. Chen, M. Hashimoto, D. Lu, A. F. Kemper, I. R. Fisher, and Z.-X. Shen, Phys. Rev. B **99**, 035118 (2019).
- [18] Matthew D. Watson, Pavel Dudin, Luke C. Rhodes, Daniil V. Evtushinsky, Hideaki Iwasawa, Saicharan Aswartham, Sabine Wurmehl, Bernd Büchner, Moritz Hoesch, Timur K. Kim, npj Quantum Materials **4**, 36 (2019).
- [19] Xingye Lu, J. T. Park, R. Zhang, H. Luo, A. H. Nevidomskyy, Q. Si, and Pengcheng Dai, Science **345**, 657 (2014).
- [20] Mingquan He, Liran Wang, Felix Ahn, Frédéric Hardy, Thomas Wolf, Peter Adelmann, Jörg Schmalian, Ilya Eremin, and Christoph Meingast, Nat. Comm. **8**, 504 (2017).
- [21] Xingye Lu, D. D. Scherer, D. W. Tam, W. Zhang, R. Zhang, H. Luo, L. W. Harriger, H. C. Walker, D. T. Adroja, B. M. Andersen, and Pengcheng Dai, Phys. Rev. Lett. **121**, 067002 (2018).
- [22] C. Dhital, Z. Yamani, W. Tian, J. Zeretsky, A. S. Sefat, Z. Wang, R. J. Birgeneau, and S. D. Wilson, Phys. Rev. Lett. **108**, 087001 (2012).
- [23] C. Dhital, T. Hogan, Z. Yamani, R. J. Birgeneau, W. Tian, M. Matsuda, A. S. Sefat, Z. Wang, and S. D. Wilson, Phys. Rev. B **89**, 214404 (2014).
- [24] Y. Song, S. V. Carr, X. Y. Lu, C. L. Zhang, Z. C. Sims, N. F. Luttrell, S. X. Chi, Y. Zhao, J. W. Lynn, and Pengcheng Dai, Phys. Rev. B **87**, 184511 (2013).
- [25] David W. Tam, Yu Song, Haoran Man, Sky C. Cheung, Zhiping Yin, Xingye Lu, Weiyi Wang, Benjamin A. Frandsen, Lian Liu, Zizhou Gong, Takashi U. Ito, Yipeng Cai, Murray N. Wilson, Shengli Guo, Keisuke Koshiishi, Wei Tian, Bassam Hitti, Alexandre Ivanov, Yang Zhao, Jeffrey W. Lynn, Graeme M. Luke, Tom Berlijn, Thomas A. Maier, Yasutomo J. Uemura, and Pengcheng Dai, Phys. Rev. B **95**, 060505(R) (2017).
- [26] T. Kissikov, R. Sarkar, M. Lawson, B. T. Bush, E. I. Timmons, M. A. Tanatar, R. Prozorov, S. L. Bud'ko, P. C. Canfield, R. M. Fernandes, and N. J. Curro, Nat. Comm. **9**, 1058 (2018).
- [27] Xingye Lu, Kuo-Feng Tseng, T. Keller, Wenliang Zhang, Ding Hu, Yu Song, Haoran Man, J. T. Park, Huiqian Luo, Shiliang Li, Andriy H. Nevidomskyy, and Pengcheng Dai, Phys. Rev. B **93**, 134519 (2016).
- [28] M. F. Collins, *Magnetic Critical Scattering* (Oxford University Press, New York, 1989).
- [29] R. J. Birgeneau, H. J. Guggenheim, and G. Shirane, Phys. Rev. B **1**, 2211 (1970).
- [30] J. Als-Nielsen, R. J. Birgeneau, H. J. Guggenheim, and G. Shirane, Phys. Rev. B **12**, 4963 (1975).
- [31] M. P. Schulhof, R. Nathans, P. Heller, and A. Linz, Phys. Rev. B **4**, 2254 (1971).
- [32] K. F. Tseng, T. Keller, A. C. Walters, R. J. Birgeneau, and B. Keimer, Phys. Rev. B **94**, 014424 (2016).
- [33] S. D. Wilson, Z. Yamani, C. R. Rotundu, B. Freelon, P. N. Valdivia, E. Bourret-Courchesne, J. W. Lynn, Songxue Chi, Tao Hong, and R. J. Birgeneau, Phys. Rev. B **82**, 144502 (2010).
- [34] Yu Li, Weiyi Wang, Yu Song, Haoran Man, Xingye Lu, Frédéric Bourdarot, and Pengcheng Dai, Phys. Rev. B **96**, 020404(R) (2017).
- [35] O. J. Lipscombe, Leland W. Harriger, P. G. Freeman, M. Enderle, Chenglin Zhang, Miaoying Wang, Takeshi Egami, Jiangping Hu, Tao Xiang, M. R. Norman, and Pengcheng Dai, Phys. Rev. B **82**, 064515 (2010).
- [36] N. Qureshi, C. H. Lee, K. Kihou, K. Schmalzl, P. Steffens, and M. Braden, Phys. Rev. B **90**, 100502 (2014).
- [37] Chong Wang, Rui Zhang, Fa Wang, Huiqian Luo, L. P. Regnault, Pengcheng Dai, and Yuan Li, Phys. Rev. X **3**, 041036 (2013).
- [38] Yu Song, Louis-Pierre Regnault, Chenglin Zhang, Guotai Tan, Scott V. Carr, Songxue Chi, A.D. Christianson, Tao Xiang, and Pengcheng Dai, Phys. Rev. B **88**, 134512 (2013).
- [39] Chenglin Zhang, Yu Song, L.-P. Regnault, Yixi Su, M. Enderle, J. Kulda, Guotai Tan, Zachary C. Sims, Takeshi Egami, Qimiao Si, and Pengcheng Dai, Phys. Rev. B **90**, 140502 (2014).
- [40] J. W. Lynn, Y. Chen, S. Chang, Y. Zhao, S. Chi, W. Ratcliff, II, B. G. Ueland, and R. W. Erwin, Journal of Research of NIST **117**, 61 (2012).
- [41] W. C. Chen, G. Armstrong, Y. Chen, B. Collett, R. Erwin, T. R. Gentile, G. L. Jones, J. W. Lynn, S. McKenney, and J. E. Steinberg, Physica B **397**, 168 (2007).
- [42] See supplementary information for additional data and analysis.
- [43] S. Avci, O. Chmaissem, J.M. Allred, S. Rosenkranz, I. Eremin, A.V. Chubukov, D.E. Bugaris, D.Y. Chung, M.G. Kanatzidis, J.-P. Castellan, J.A. Schlueter, H. Claus, D.D. Khalyavin, P. Manuel, A. Daoud-Aladine, and R. Osborn, Nat. Comm. **5**, 3845 (2014).
- [44] J. M. Allred, K. M. Taddei, D. E. Bugaris, M. J. Krogstad, S. H. Lapidus, D. Y. Chung, H. Claus, M. G. Kanatzidis, D. E. Brown, J. Kang, R. M. Fernandes, I. Eremin, S. Rosenkranz, O. Chmaissem, and R. Osborn, Nat. Phys. **12**, 493 (2016).
- [45] Daniel D. Scherer and Brian M. Andersen, Phys. Rev. Lett. **121**, 037205 (2018).
- [46] M. Nakajima, T. Liang, S. Ishida, Y. Tomioka, K. Kihou, C. H. Lee, A. Iyo, H. Eisaki, T. Kakeshita, T. Ito, and S. Uchida, PNAS **108**, 12238 (2011).
- [47] Xiao Ren, Lian Duan, Yuwen Hu, Jiarui Li, Rui Zhang, Huiqian Luo, Pengcheng Dai, and Yuan Li, Phys. Rev. Lett. **115**, 197002 (2015).
- [48] A. Baum, Ying Li, M. Tomić, N. Lazarević, D. Jost, F. Löffler, B. Muschler, T. Böhm, J.-H. Chu, I. R. Fisher, R. Valenti, I. I. Mazin, and R. Hackl, Phys. Rev. B **98**, 075113 (2018).
- [49] All raw data from ILL will be published at DOI:10.5291/ILL-DATA.4-02-531, and from NCNR will be provided upon request.

- [50] Gen Shirane, Stephen M. Shapiro, and John M. Tranquada, Neutron Scattering with a Triple-Axis Spectrometer, Cambridge University Press 2004, p.170.

ACKNOWLEDGEMENTS

The work at BNU is supported by the NSFC under Grant No. 11734002 and 11922402. The work at Rice University is supported by the U.S. NSF DMR-1700081 and the Robert A. Welch Foundation Grant No. C-1839 (P.D.). The work at UCB was supported by the U.S. DOE BES under Contract No. DE-AC02-05-CH11231 within the Quantum Materials Program (KC2202).

AUTHOR CONTRIBUTIONS

P.D. and X.L. conceived the project. P.L., M.L.K., L.T., G.T. and X.L. prepared the samples. Polarized inelastic neutron scattering experiments at IN22 were carried out by P.L., L.T., X.L., K.S., J.T.P., Y.L., Y.S., and F. B. Neutron diffraction measurements at BT-7 were carried out by M.L.K, Y.S., D.W.T., J.W.L, Y. Z., and R.J.B. The entire project was supervised by P.D. The manuscript was written by P.D., P.L., X.L. and Y.S. All authors made comments.